J Adv Ceram

Research Article

Synergistic improvement of the mechanical and biological performance of Si_3N_4 by incorporating nanostructured graphene

Zhe Zhan[1,†], Bin Deng[2,†], Yanru Chen[2], Xinghong Zhang[3], Jinzhu Song[1,✉]

Cite this article: Zhan Z, Deng B, Chen Y, et al. *J Adv Ceram* 2025, **14**(2): 9221026. https://doi.org/10.26599/JAC.2024.9221026

ABSTRACT: Achieving synergy between mechanical and biological performance has long been a challenge in developing silicon nitride (Si_3N_4) as a bone regeneration implant material. In this study, a nanostructured graphene-toughened Si_3N_4 composite (Si_3N_4–G) was prepared, and the mechanical and biological properties of the resulting Si_3N_4–G composite were compared with those of Si_3N_4 ceramics without graphene addition. The incorporation of nanostructured graphene substantially improves the mechanical properties of Si_3N_4. Furthermore, the nanoscale thickness of graphene enhances antibacterial activity through a "cutting" effect, while its high specific surface area promotes cell adhesion, activating mechanosensitive pathways linked to osteogenic differentiation. This work provides new insights into the potential applications of Si_3N_4-based bio-ceramics in bone tissue engineering.

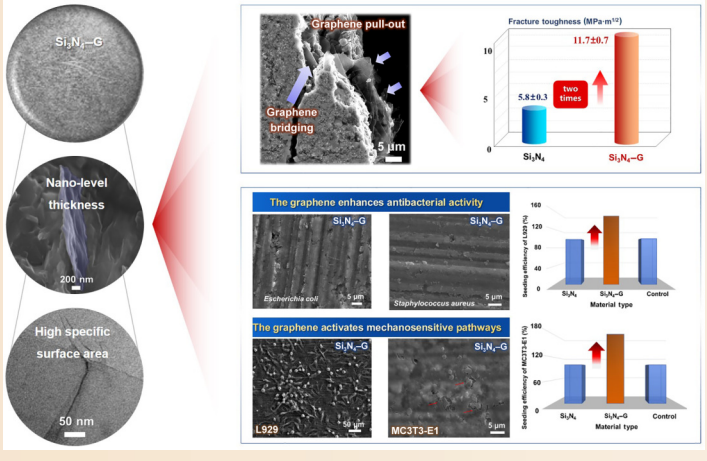

KEYWORDS: silicon nitride (Si_3N_4); graphene (G); mechanical properties; biocompatibility

1 Introduction

The use of implant materials is becoming increasingly critical for repairing or reconstructing damaged physiological functions, particularly in hard bone tissue engineering [1,2]. For successful implantation, materials must exhibit not only reliable mechanical properties but also high tissue compatibility, low cytotoxicity, and robust antibacterial characteristics. Recently, Si_3N_4-based bio-ceramics, known for their high strength and good biocompatibility, have gained increasing attention in clinical bone implant surgeries and are considered ideal candidates for bone implants [3–6].

One of the main issues that limits the widespread application of Si_3N_4-based bio-ceramics is the integration of their mechanical and biological performance [7]. As a traditional engineering structural ceramic, Si_3N_4 has been extensively studied, with a special emphasis on enhancing the fracture toughness by using various additives, such as boron nitride (BN) [8,9], silicon carbide (SiC) [10], tungsten carbide (WC) [11], carbon nanotubes [12], diamond [13], and metals [14]. However, these additives can negatively impact biocompatibility or antibacterial properties, making them unsuitable for human implant applications [12–15]. An alternative approach is urgently required to guarantee fracture toughness while enhancing biological activity [16–19].

Graphene (G), as a novel low-dimensional nanomaterial, possesses a distinct two-dimensional structure with a high specific surface area, exceptional mechanical properties, and promising antibacterial activity [20,21]. These unique characteristics make graphene an excellent reinforcement material for potentially improving fracture toughness without compromising the biocompatibility of brittle bio-ceramics. Despite these promising attributes, challenges remain in effectively integrating graphene into Si_3N_4 to achieve the desired balance of mechanical and biological performance. If graphene is directly compounded with Si_3N_4, the agglomeration problem emerges as a significant challenge. Owing to their high surface energy and strong van der

† Zhe Zhan and Bin Deng contributed equally to this work.

[1] School of Life Science and Technology, Harbin Institute of Technology, Harbin 150001, China. [2] Department of Stomatology, the First Medical Center, Chinese PLA General Hospital, Beijing 100853, China. [3] Center for Composite Materials and Structures, Harbin Institute of Technology, Harbin 150001, China.

✉ Corresponding author. E-mail: sjz@hit.edu.cn

Received: January 28, 2024; Revised: December 7, 2024; Accepted: December 27, 2024

Waals forces [21], the graphene particles tend to adsorb to each other and form agglomerates during the compounding process. This agglomeration not only reduces the strength and toughness but also adversely affects the biocompatibility, weakens antibacterial properties, and limits nutrient delivery, thereby impacting the biological applications of the resultant composite. Therefore, addressing the agglomeration issue is crucial for enhancing the performance of silicon nitride incorporated with graphene.

Graphene oxide, as the oxidized form of graphene, retains similar properties to those of graphene and features oxygen-containing functionalities that enhance surface activity and hydrophilicity [22–24], facilitating uniform dispersion in a Si_3N_4 slurry and avoiding agglomeration. Additionally, the conversion of graphene oxide to graphene can be achieved through high-temperature treatments (600–1000 °C) [25]. In this study, graphene oxide was utilized to prepare the graphene-toughened silicon nitride (Si_3N_4) composite. The focus was on evaluating and discussing the resultant mechanical and biological properties of the composite, with the ultimate goal of enhancing the applicability of Si_3N_4 bio-ceramics in hard bone tissue engineering. This research provides valuable insights into the performance of graphene-toughened Si_3N_4 composites, paving the way for their effective implementation in regenerative medicine and orthopedic applications.

2 Experimental

α-Si_3N_4 powders (99.9% purity, average particle size of 600 nm), and Al_2O_3 and Y_2O_3 sintering additives (99.9% purity, average particle size of 500 nm) were purchased from Beijing HWRK Chem Co., Ltd., China. Graphene oxide (GO) with an average particle size of 500 nm and purity greater than 99% was purchased from Suzhou TanFeng Graphene Technology Co., Ltd., China. The powder mixtures (93 wt% Si_3N_4, 5 wt% Al_2O_3, and 2 wt% Y_2O_3) with 5 wt% GO were ball-milled (using ethanol as the solvent and Si_3N_4 as the milling ball) at 300 r/min for 8 h to obtain well-mixed ceramic slurries. The slurries were dried in a rotary evaporator at 70 °C with a rotation speed of 35 r/min under vacuum. The dried powders were spark-plasma-sintered at 1700 °C/50 MPa for 600 s under vacuum with heating and cooling rates of 100 and 30 °C/min, respectively, to prepare nano-graphene toughened Si_3N_4 composites (Si_3N_4–G). For comparative purposes, Si_3N_4–Al_2O_3–Y_2O_3 without graphene (Si_3N_4) was prepared with the same processing parameters.

The bulk density of the sintered samples was determined using the Archimedes drainage method. The samples were machined to dimensions of 3 mm × 4 mm × 20 mm to measure the flexural strength using an Instron-5500 unit with a span of 16 mm and a loading rate of 0.5 mm/min. The fracture toughness was tested with the single-edge notched beam (SENB) method with a 16 mm span and crosshead speed of 0.05 mm/min with 2 mm × 4 mm × 22 mm test bars. A scanning electron microscope (SEM; SU5000, Hitachi, Japan) coupled with energy dispersive spectroscopy (EDS) was used to investigate the sample microstructure, surface composition, and fractographs. An X-ray diffractometer (XRD; X′ PERT PRO MPD, Panalytical, the Netherlands) was also utilized to analyze the sample composition.

Staphylococcus aureus (*S. aureus*; ATCC 12598) and *Escherichia coli* (*E. coli*; ATCC 25922) were incubated in Luria broth (LB) medium (Sigma-Aldrich, USA) for 12 h to prepare a fresh bacterial suspension. Sterilized Si_3N_4 and Si_3N_4–G were submerged in a bacterial suspension with a cell density of 1×10^5 cells/mL at 37 °C for 24 h. The Acridine orange/ethidium bromide (AO/EB) double staining kit obtained from Shanghai Yuanye Bio-Technology Co., Ltd., China, was used to assess the viability of bacteria adhered to the surfaces of Si_3N_4 and Si_3N_4–G. An inverted fluorescence microscope (IX71, Olympus, Japan) was employed to image the bacteria and determine their viability. The microstructure of the adhered bacteria was analyzed by SEM.

L929 mouse fibroblasts and MC3T3-E1 osteoblasts, purchased from Procell Life Science & Technology Co., Ltd., were cultured in high-glucose Dulbecco's modified Eagle medium (DMEM, Gibco, Germany) supplemented with 10% fetal bovine serum (FBS, Sigma, USA) at 37 °C with 5% CO_2 to examine the behavior of cells on the surface of sterilized Si_3N_4 and Si_3N_4–G. L929 and MC3T3-E1 cells at a density of 10^4 cells/mL were incubated in the medium supplemented with extracted Si_3N_4 or Si_3N_4–G for 24 h. 3-(4,5-Dimethylthiazol-2-yl)-2,5-diphenyltetrazolium bromide (MTT) assay kit (Solarbio, China) was used to determine *in vitro* cytotoxicity. A calcein-AM/propidium iodide (PI) double stain kit (Solarbio, Beijing, China) was employed in live/dead cell staining to assess viability. The live cells appeared as calcein-AM-stained green, and the dead cells were PI-stained red. The inverted fluorescence microscope was utilized to image the resulting staining. L929 and MC3T3-E1 cells at a density of 1×10^5 cells/mL in growth media (GM) were added to Si_3N_4 and Si_3N_4–G and grown at 37 °C in 5% CO_2. Cell counting kit-8 (CCK-8; Dojindo, Japan) was used to evaluate cell viability. Each sample loaded with cells was submerged in 0.5 mL GM enriched with 10% CCK-8 solution. After 1, 3, and 7 d of incubation, the absorbance of the supernatant at 405 nm was determined using a Hitachi U-3900 spectrophotometer (Japan). L929 and MC3T3-E1 cells at a density of 2×10^4 cells/mL were added to various samples, and the microstructures of the cells were analyzed by SEM. Double labeling with fluorescein isothiocyanate–phalloidin (FITC–phalloidin) and 4',6-diamidino-2-phenylindole (DAPI) was used to clarify the actin cytoskeleton of fibroblasts; a confocal laser scanning microscope (CLSM; LSM 880, ZEISS, Germany) was employed for image analysis.

MC3T3-E1 cells were seeded onto Si_3N_4 and Si_3N_4–G at a density of 5×10^4 cells/mL. After 24 h, the culture medium was changed to an osteogenesis inductive medium (Solarbio, China). The cells were induced osteogenically for 7, 14, or 21 d, and osteogenic cell differentiation was assessed using the alkaline phosphatase (ALP) activity assay kit (Beyotime, China). The ALP activity and total protein content of the cells were determined by staining and quantitatively assessed. After cultivation for 21 d, the alizarin red staining assay (ARS, Solarbio, China) was used to evaluate calcium-rich deposits. The total RNA content of the cells co-cultured for 7, 14, and 21 d in the osteogenic induction medium was determined using the Trizol reagent (Invitrogen, USA). Reverse transcription was conducted using the HiScript II Q Select RT SuperMixkit (Vazyme, China). The AceQ Universal SYBR qPCR Master Mix (Vazyme, China) and primers specific for 6 gene markers were used for quantitative real-time polymerase chain reaction (PCR) analysis to evaluate the expression levels of osteogenic genes [17–19]: alkaline phosphatase (ALP), collagen type-1 (COL-1), osteocalcin (OCN), osteopontin (OPN), osteorotegerin (OPG), runt-related transcription factor 2 (RUNX2), and glyceraldehyde 3-phosphate dehydrogenase. Glyceraldehyde-3-phosphate dehydrogenase (GAPDH) served as the internal control for mRNAs.

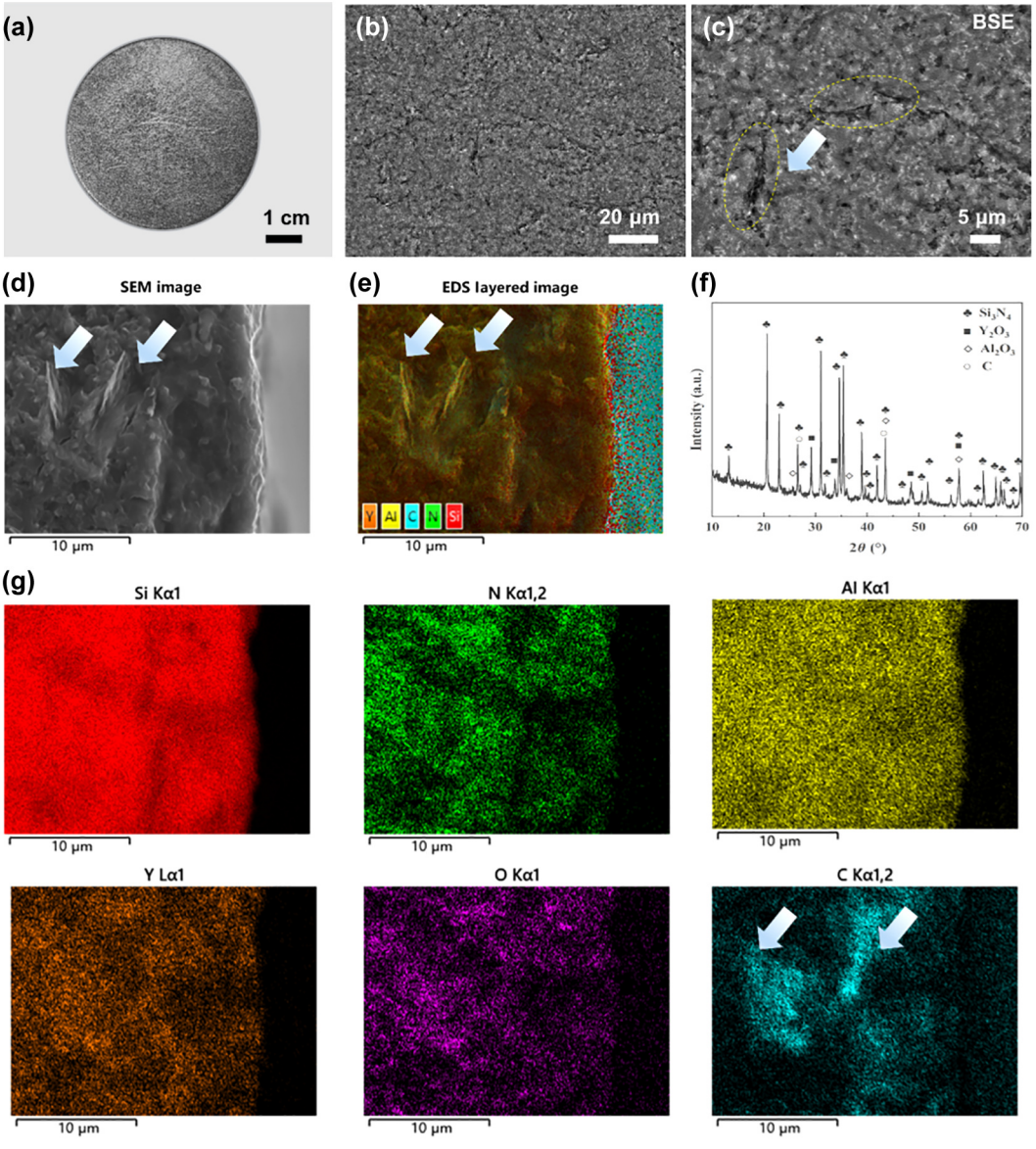

Fig. 1 Microstructures and compositions of Si_3N_4–G composite: (a) macroscopic features; (b, c) representative SEM images; (d, e) representative BSE images; (f) XRD pattern; (g) EDS elemental maps.

3 Results and discussion

3.1 Microstructure

The microstructure and composition of the Si_3N_4–G composite are presented in Fig. 1. The image presented in Fig. 1(a) does not exhibit any discernible pores or cracks at the macroscopic level. The SEM images (Figs. 1(b) and 1(c)) reveal a smooth surface with no evidence of pores. These images suggest that the graphene additive is homogeneously distributed in the Si_3N_4 ceramics. The corresponding backscattered electron (BSE) images (Figs. 1(d) and 1(e)) reveal black flakes (graphene, indicated by the blue arrow) and a gray matrix (Si_3N_4) that represent a uniform distribution of both phases. The XRD pattern for the Si_3N_4–G composite (Fig. 1(f)) shows peaks attributed to Si_3N_4, Y_2O_3, Al_2O_3, and C. Figure 1(g) shows the results of corresponding EDS analysis. Si, N, Y, Al, O, and C are evenly dispersed across the sample area, and the graphene structure can be distinguished from the C elemental map. The observed distributions of graphene, Si_3N_4, and sintering additives are important in determining the ultimate composite performance.

GO was reduced to G at 1700 °C in an inert atmosphere, followed by hot pressing at 50 MPa for 600 s. This treatment removed oxygen groups from GO [25], restoring its graphene structure and promoting uniform distribution within Si_3N_4 matrix, enhancing composite densification and mechanical properties. The XRD pattern (Fig. 1(f)) exhibits characteristic diffraction peaks of graphene, with no evident peaks corresponding to by-products of oxidation, indicating the complete reduction of GO into graphene under the applied conditions. SEM images (Figs. 1(b) and 1(c)) and BSE images (Figs. 1(d) and 1(e)) reveal that graphene is uniformly distributed in the matrix in the form of flake-like structures, highlighting its two-dimensional nanostructural characteristics. Furthermore, the uniform distribution of carbon observed in the EDS elemental maps (Fig. 1(g)) corroborates the flake-like morphology of

graphene, demonstrating its well-dispersed and structurally intact state within the Si_3N_4 matrix. These results collectively confirm the successful conversion of GO to nanostructured graphene, which is uniformly integrated within the Si_3N_4 matrix under the specified processing conditions.

3.2 Mechanical properties

The load–displacement curves measured during strength tests with Si_3N_4 and Si_3N_4–G composites are given in Fig. 2, each showing the results for five samples. For Si_3N_4 (Fig. 2(a)), the load increases with displacement and reaches a maximum before a "sudden decline", indicating rapid fracture after the material reaches its load limit, approximately 130 N. On the other hand, the curves measured with Si_3N_4–G (Fig. 2(b)) show a load limit of approximately 180 N, and the displacement extends beyond 0.08 mm before a "gentle decline" occurs. Compared with the samples without graphene, the material with graphene demonstrates higher toughness and energy absorption capacity before fracture. The "gentle decline" appearing in the curves indicates that the material with graphene has some plastic deformation ability after reaching the load limit, reducing the risk of sudden fracture and exhibiting better damage tolerance. The addition of graphene increases the load limit by approximately 50% and extends the displacement limit, indicating a significant improvement in crack resistance and toughness. The measured fracture toughness increases from 5.8±0.3 MPa·m$^{1/2}$ for Si_3N_4 to 11.7±0.7 MPa·m$^{1/2}$ for Si_3N_4–G, demonstrating the positive role of graphene in enhancing the toughness of the material. Moreover, the Si_3N_4–G composite maintains a high flexural strength (455.4±19.4 MPa) and compressive strength (2178.1±41.1 MPa). This combination of high toughness and high strength signifies a notable advancement in reliability for applications requiring compatibility with hard bone tissue.

The crack paths in the samples of Si_3N_4 and Si_3N_4–G are shown in Fig. 3. For Si_3N_4 sample (Fig. 3(a)), the crack penetrates along a straight line through the interior of the material. This brittle

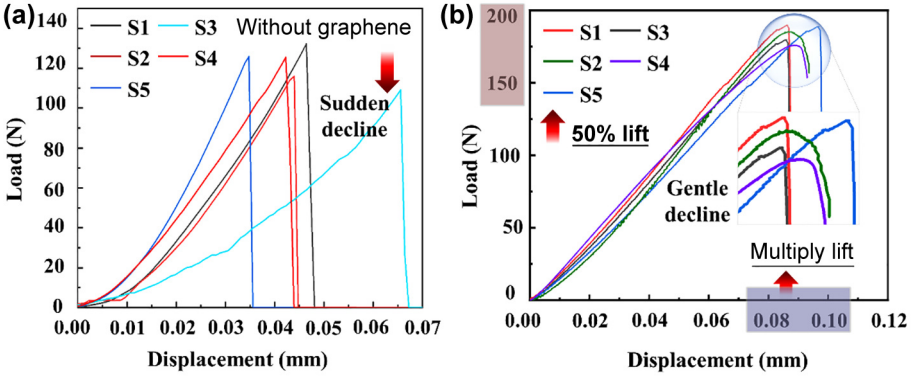

Fig. 2 Load–displacement curves for (a) Si_3N_4 and (b) Si_3N_4–G. S-1–S-5 represent 5 valid samples.

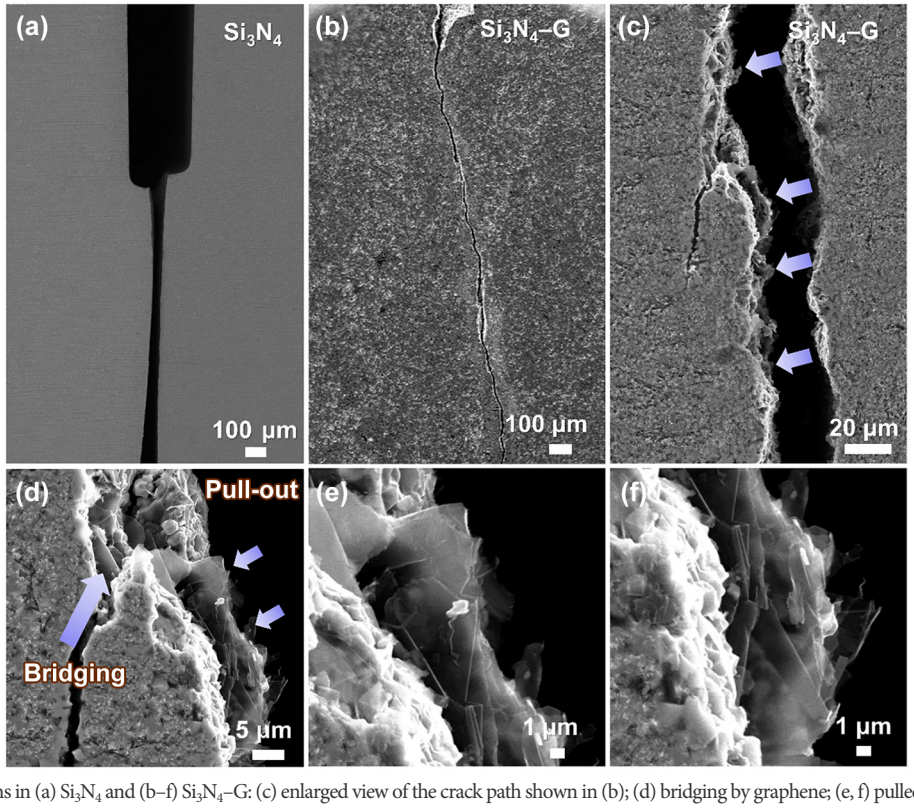

Fig. 3 Crack paths in (a) Si_3N_4 and (b–f) Si_3N_4–G: (c) enlarged view of the crack path shown in (b); (d) bridging by graphene; (e, f) pulled-out of graphene.

fracture mode is usually accompanied by large crack-opening displacements, indicating rapid failure of the material under stress. For Si_3N_4–G sample, the introduction of graphene significantly changes the crack propagation behavior. The inclusion of graphene results in a more tortuous crack path with a smaller gap (Fig. 3(b)). Crack deflection and branching can be observed along the crack path (Fig. 3(c)). In Si_3N_4–G, fracture of Si_3N_4 and graphene occurred alternately owing to the clear difference in modulus between the two phases. The simultaneous bridging by graphene (Fig. 3(d)) and pulled-out of graphene (Figs. 3(e) and 3(f)) result in a narrower crack opening with a tendency towards crack closure.

It is of interest to investigate the effect of the morphology of graphene on the toughening behavior of Si_3N_4 matrix. Figure 4 shows the occurrence of surface tearing-off as a fracture feature observed in Si_3N_4–G. When being viewed under higher magnification, graphene exhibits a nano-scale thickness and a micron-scale length (Fig. 4(a)), as well as a high aspect ratio and high specific surface area (Fig. 4(b)). These features may contribute to energy dissipation during crack propagation, resulting in a higher fracture toughness of Si_3N_4–G.

A schematic diagram of the toughening mechanisms of graphene is shown in Fig. 5. The toughening mechanisms of graphene in silicon nitride ceramics work together to greatly improve the ’fracture resistance of the material. The pull-out effect reduces stress at the crack tip by pulling graphene sheets from the matrix as cracks advance, which dissipates energy and slows crack growth. Graphene bridging helps toughen the material by spanning cracks, redistributing stress, and delaying crack propagation. When cracks encounter graphene, crack deflection and branching occur due to the mismatch in properties between graphene and ceramics, forcing cracks to take longer, more complex paths, which consumes more energy. The strong interfacial interaction between graphene and the ceramic matrix prevents cracks from easily penetrating and instead promotes deflection, increasing the toughness. Finally, the modulus mismatch between graphene and the matrix acts as a flexible barrier that slows crack growth, further boosting the ’fracture resistance of the material. Together, these mechanisms significantly increase the toughness and durability of the composite.

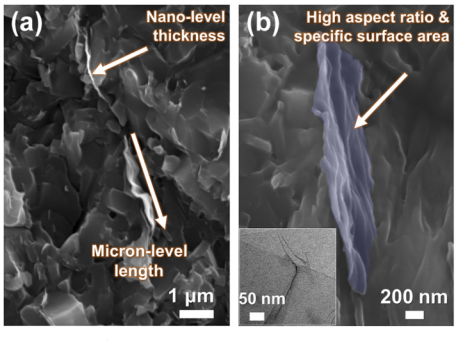

Fig. 4 Micrographs of (a) nano-level thickness and micro-level length and (b) high aspect ratio and high specific surface area of graphene in Si_3N_4–G.

3.3 Biological performance

To directly evaluate antimicrobial activity, the metabolic responses of *S. aureus* ATCC 12598 and *E. coli* ATCC 25922 were determined, and the results are presented in Fig. 6. The bacterial staining of Si_3N_4 showed a wider region of green fluorescence (Figs. 6(a) and 6(e)), demonstrating that the eluted bacteria maintained viability. Both *S. aureus* and *E. coli* displayed a larger area of red staining for Si_3N_4–G, indicating a relatively large number of dead bacteria (Figs. 6(d) and 6(h)). These results clearly indicated that the bacterial suspension eluted from the surface of Si_3N_4–G exhibited lower bacterial activity. The SEM images of *S. aureus* and *E. coli* bacterial adherence to the surfaces of Si_3N_4 and Si_3N_4–G after culture for 24 h are shown in Figs. 6(i)–6(l). Appreciable concentrations of *S. aureus* and *E. coli* were viable on the surface of Si_3N_4 (Figs. 6(i) and 6(k)). Only a few bacteria were collected from the surface of the Si_3N_4–G composites (Figs. 6(j) and 6(l)). Since the number of bacteria attached to the surface is directly related to antibacterial effectiveness, our results demonstrate that the addition of graphene effectively improves the antibacterial performance of Si_3N_4.

The observed increase in antibacterial activity is dependent on the physical and chemical characteristics of graphene [26,27]. The graphene with the microstructure of nano-level thickness and micron-level length (Fig. 4(a)) can effectively penetrate bacteria, destroying the cell wall and membrane structure. Moreover, graphene penetration results in the destruction of nucleic acids

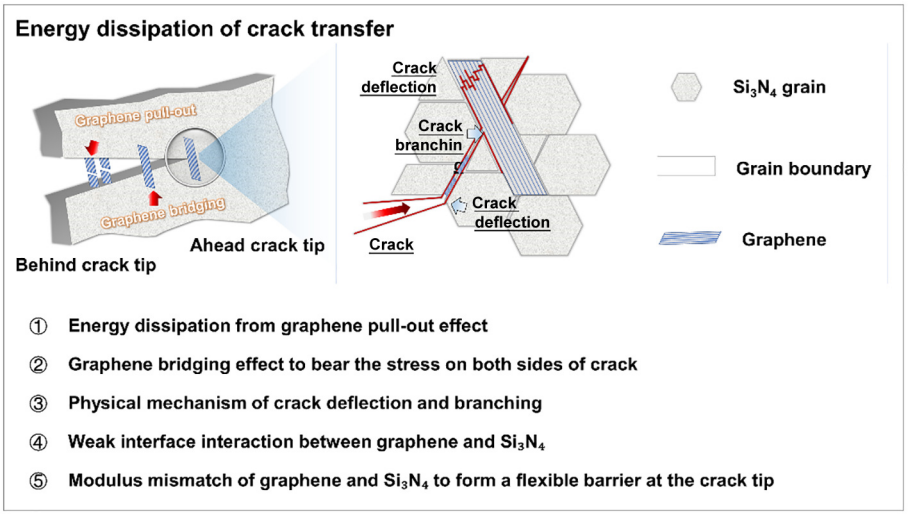

Fig. 5 Toughening mechanisms of graphene to Si_3N_4.

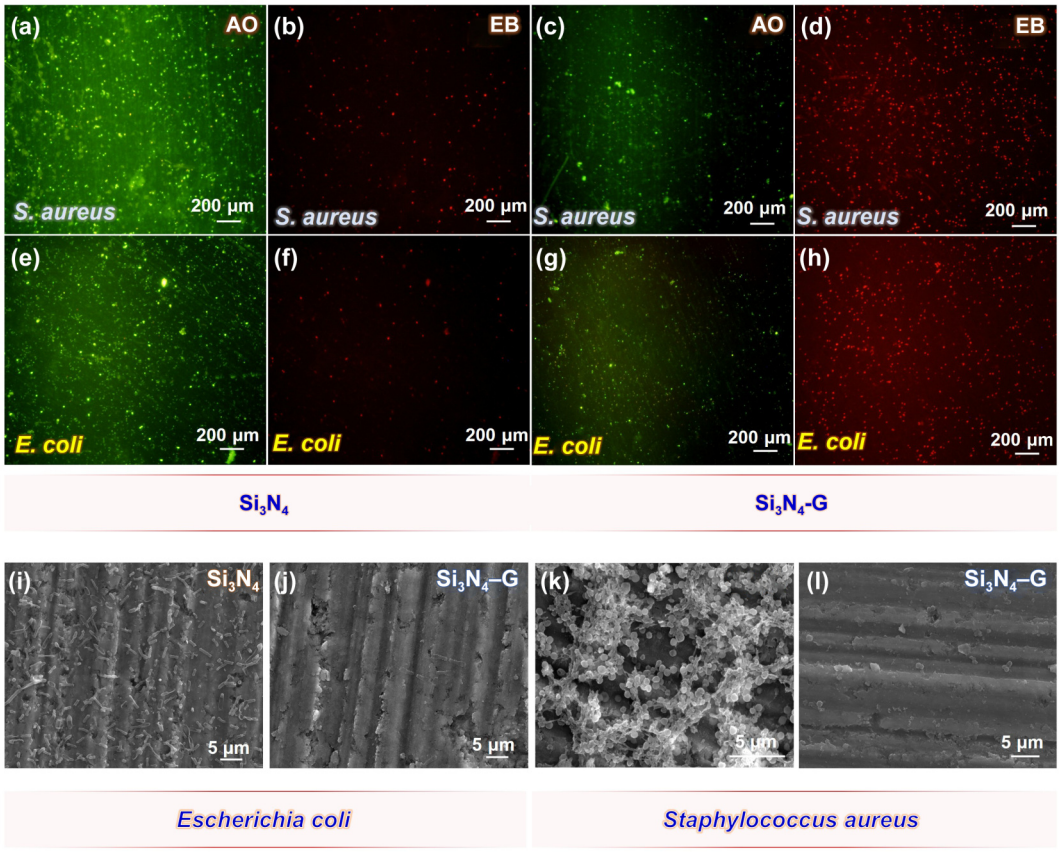

Fig. 6 Live/dead staining images and SEM images of *S. aureus* and *E. coli* adhered to the surfaces of Si_3N_4 and Si_3N_4–G: (a, b, e, f) staining images for Si_3N_4; (c, d, g, h) staining images for Si_3N_4–G; (i) *E. coli* on Si_3N_4; (j) *E. coli* on Si_3N_4–G; (k) *S. aureus* on Si_3N_4; (l) *S. aureus* on Si_3N_4–G.

and proteins in the cytoplasm, ultimately leading to bacterial death [28]. The high aspect ratio and specific surface area of graphene (Fig. 4(d)) trap and isolate bacteria from the surrounding medium, hindering their proliferation [29,30]. In addition, the oxidative stress induced by graphene can cause bacterial cell inactivation; that is, the production of reactive oxygen species (ROS) results in lipid peroxidation, leading to metabolic disorders, cell membrane damage, and bacterial death [31,32].

The MTT assay was used to identify the *in vitro* cytotoxicity of the materials and was combined with live/dead staining analysis to assess the survival state of cells on the surface of Si_3N_4 and Si_3N_4–G. The material extracts were chosen for co-cultured cell plating of L929 and MC3T3-E1. The quantitative results revealed that both materials exhibited a high cell seeding survival rate (> 100%), where the cell seeding efficiency of Si_3N_4–G was more than 50% greater than that of Si_3N_4 (Fig. 7(a)). The results of live and dead cell staining (Fig. 7(b)) showed larger areas of strong green fluorescence both on the surface of Si_3N_4 and Si_3N_4–G. Moreover, a wide oval shape of L929 cells and a long spindle structure of MC3T3-E1 cells were found on the surface of Si_3N_4–G. This could reflect better cell survival and higher cytocompatibility of Si_3N_4–G than Si_3N_4. The CCK-8 test was performed to assess the impacts of Si_3N_4 and Si_3N_4–G on cell proliferation, and the results are shown in Fig. 7(c). The relative proliferation of L929 and MC3T3-E1 cells on both surfaces increased with time. There was no apparent difference between the two groups on days 1 and 4. On day 7, the relative proliferation of both cell lines on Si_3N_4–G was clearly higher (60% higher for L929 and 90% higher for MC3T3-E1 cells) than that on Si_3N_4.

The adhesion microstructures of L929 and MC3T3-E1 cells on both Si_3N_4 and Si_3N_4–G are shown in Fig. 8. After culturing for 24 h, L929 fibroblasts exhibited a typical spindle morphology on both surfaces (Figs. 8(a) and 8(b)). At higher magnification, the cell nucleus associated with Si_3N_4–G was fuller, presenting an oval shape (Fig. 8(b)). Moreover, the cells were arranged more closely over a larger area with better differentiation and extension, suggesting that cell adhesion is stronger on the surface of Si_3N_4–G. The MC3T3-E1 cells distributed on the surface of Si_3N_4 exhibited a spherical morphology, with some evidence of stretching and presence of smaller spindle shapes (Fig. 8(c)). The MC3T3-E1 cells adhered to Si_3N_4–G showed a flatter structure with extended actin microfilaments and evidence of cluster-like fusion (Fig. 8(d)), suggesting that interaction with Si_3N_4–G results in significant expansion and extension of the cell membrane. The higher adsorption area of Si_3N_4–G results in greater differentiation capability. Graphene inclusion plays a key role in promoting the adhesion, spreading, and proliferation of L929 and MC3T3-E1 cells. The larger surface area and roughness of graphene (Fig. 4) promoted cell adsorption and triggered mechanosensitive pathways related to osteogenic differentiation. In addition, the strong non-covalent π–π bonding of graphene and possible interactions with different biomolecules can enhance the local bioavailability of these compounds, enhancing cell differentiation [33,34].

In addition, we stained the cytoskeleton and nucleus using fluorescent phalloidin–DAPI to image the intracellular microfilaments adhered to Si_3N_4 and Si_3N_4–G. As shown in Fig. 9, both Si_3N_4 and Si_3N_4–G supported the growth of L929 and

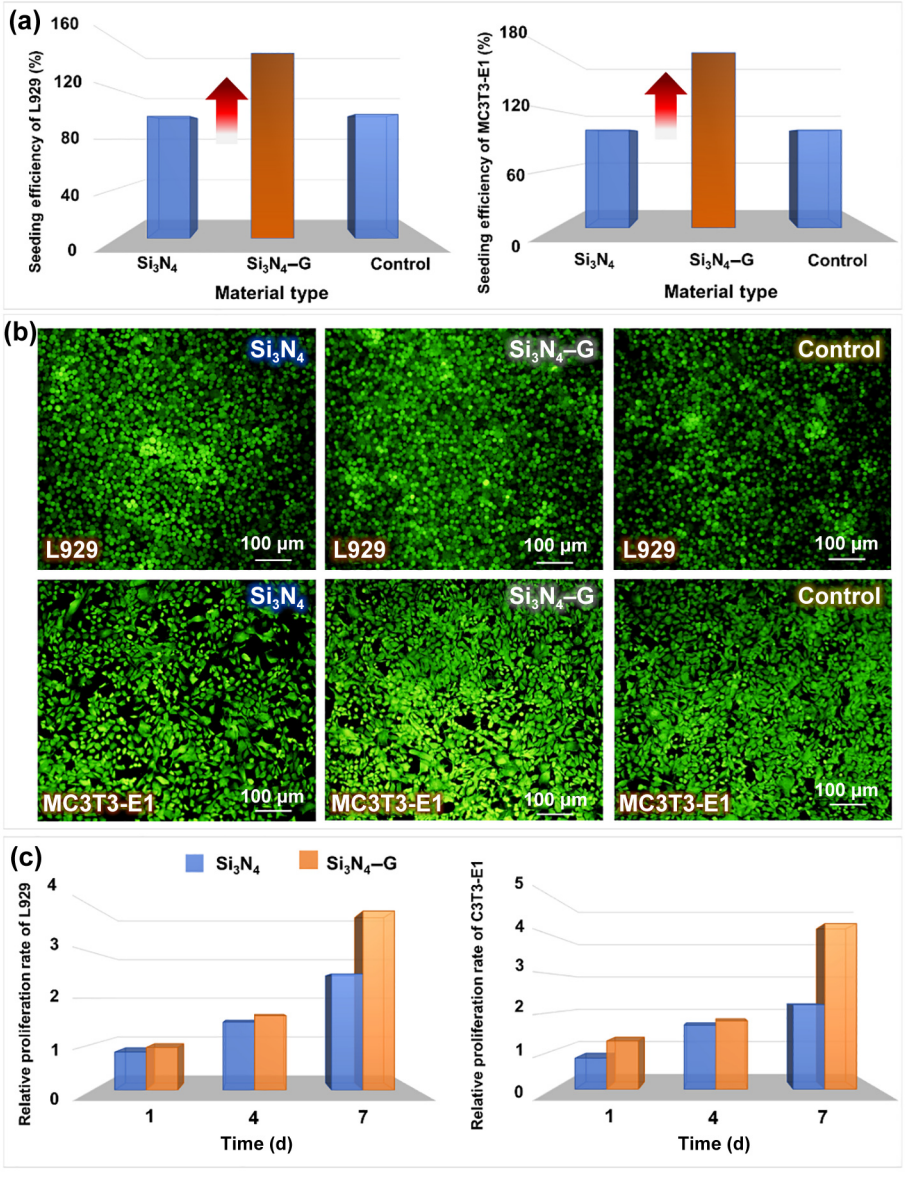

Fig. 7 *In vitro* cytotoxicity assay and live/dead cell staining image analysis: (a) initial seeding efficiency of cells; (b) live/dead cell staining of different extracts; (c) relative proliferation rates of cells after 1, 4, and 7 d.

MC3T3-E1 cells after co-cultivation for 24 h. However, both types of cells that adhered to the Si_3N_4–G substrate were more effective than those that adhered to the Si_3N_4 substrate. The cells on the Si_3N_4–G surface exhibited a more flattened morphology with a greater number of protruding actin microfilaments that form multilayers. The cytoskeletal fibers were more pronounced for cells fused in clusters. These observations support the assay results presented in Fig. 7 and the SEM images shown in Fig. 8; that is, the addition of graphene promotes the growth and proliferation of MC3T3-E1 osteoblasts and L929 murine fibroblasts on the composite surface.

MC3T3-E1 pre-osteoblast stem cells can differentiate into osteoblasts and are utilized as model cells in differentiation research. To further assess the osteogenic activity of Si_3N_4 and Si_3N_4–G, the ALP activity was measured, and Alizarin red detection was conducted to determine the early differentiation capability of osteoblasts. The results are presented in Fig. 10. After 7 d, there was little difference between the relative ALP activities exhibited by Si_3N_4 and Si_3N_4–G (Fig. 10(a)). After 14 and 21 d, the relative ALP activity of Si_3N_4–G was more than 70% and 25% higher than that of Si_3N_4, respectively. These data suggest that osteoblasts on the surface of Si_3N_4–G are in a higher differentiated state. The Alizarin red quantitative analysis shown in Fig. 10(b) revealed that the degree of cell mineralization on Si_3N_4–G was nearly 60% higher than that on Si_3N_4, which is consistent with the stained images of the mineralized nodule on day 28. These results revealed that the introduction of graphene significantly enhanced the early induction differentiation ability of osteoblasts. The real-time quantitative PCR data for 6 osteogenesis genes in MC3T3-E1 cells (Figs. 10(c)–10(h)) support the beneficial effect of graphene inclusion.

After 7, 14, and 21 d, gene expression was significantly improved compared with that in the initial stage of induced differentiation, especially after 21 d of differentiation culture. Notably, the mRNA expression levels of all 6 osteoblast-related genes on the surface of Si_3N_4–G were all higher than those on the surface of Si_3N_4 at each time point. Since the expression of genes is associated with osteogenesis, the introduction of graphene into

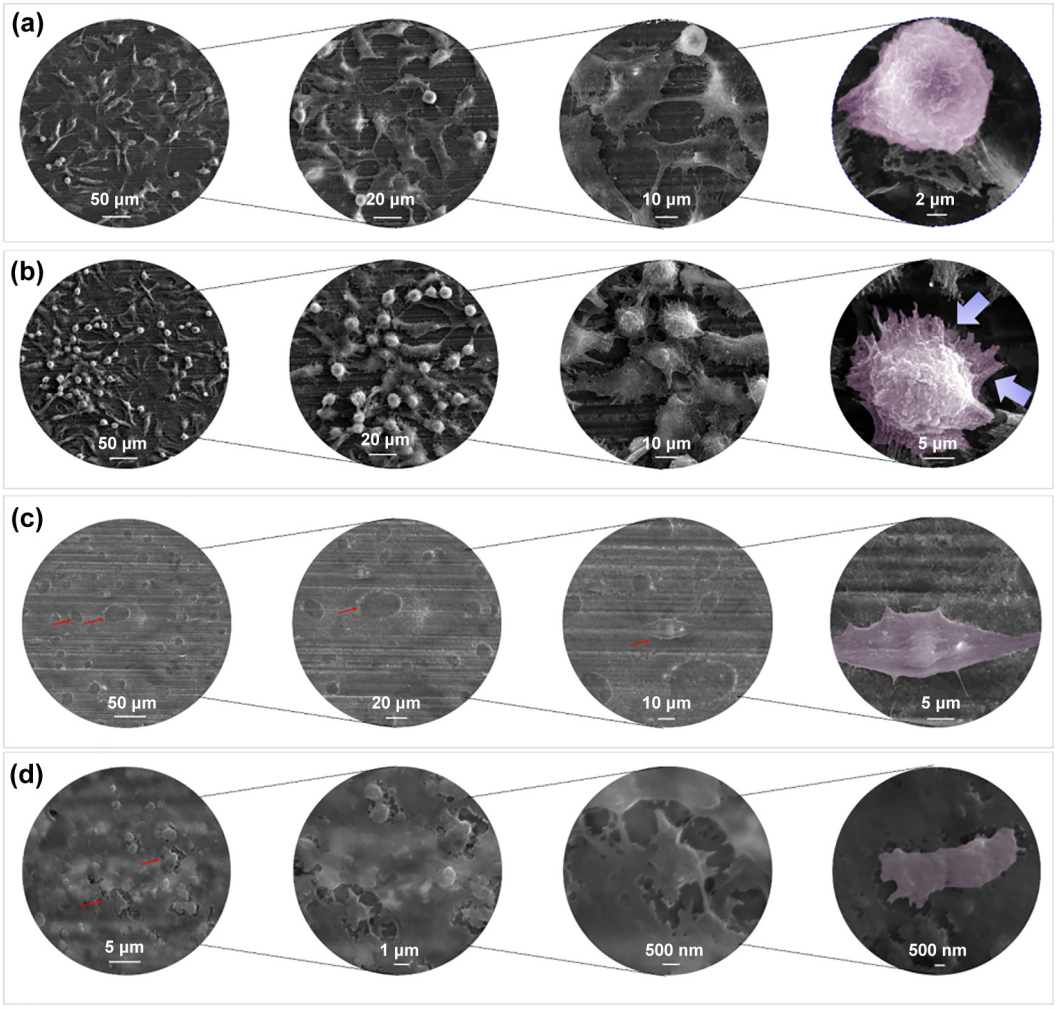

Fig. 8 SEM images showing microstructure of L929 cells on surface of (a) Si_3N_4 and (b) Si_3N_4–G and MC3T3-E1 cells on surface of (c) Si_3N_4 and (d) Si_3N_4–G.

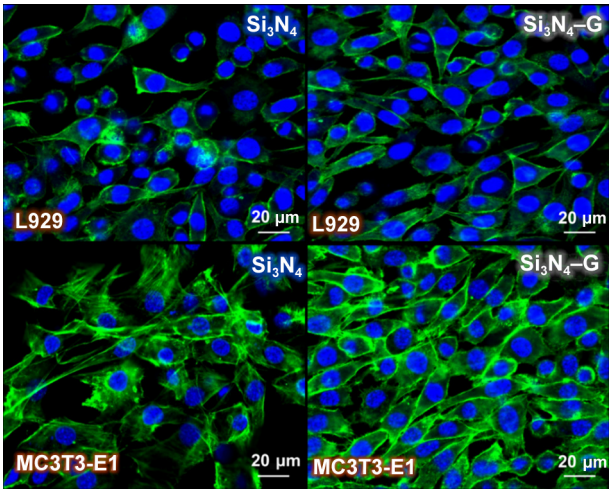

Fig. 9 Fluorescent staining of L929 and MC3T3-E1 cells with FITC–phalloidin (actin cytoskeleton, green) and DAPI (nucleus, blue).

Si_3N_4 results in a considerable increase in biological osteogenic activity.

4 Conclusions

In this work, a nanostructured graphene-toughened Si_3N_4 composite (Si_3N_4–G) was prepared. The incorporation of nano-graphene resulted in improved mechanical and biological performance. The main conclusions are as follows:

(1) The occurrence of the pull-out of graphene with a high aspect ratio and rough surface assists energy dissipation associated with crack propagation. The observed graphene bridging results in smaller crack openings and a tendency for crack closure. Consequently, the fracture toughness of Si_3N_4–G, 11.7±0.7 MPa·$m^{1/2}$, is approximately two times that of Si_3N_4. In addition, the flexural strength and compressive strength reach 455.4±19.4 and 2178.1±41.1 MPa, respectively.

(2) The cutting effect due to the nano-scale thickness of graphene results in an enhanced antibacterial activity of Si_3N_4–G. Graphene surface roughness also promotes cell adsorption and triggers mechanosensitive pathways related to osteogenic differentiation. As a result, the inclusion of graphene improves the adhesion and proliferation of L929 and MC3T3-E1 cells and also promotes the induction of osteoblast differentiation. After 7 d, the relative proliferation of both cell types on the surface of Si_3N_4–G is appreciably higher (60% higher for L929 and 90% higher for MC3T3-E1) than that of Si_3N_4. After 14 d, the relative ALP activity recorded for Si_3N_4–G is over 70% higher than that for Si_3N_4. The mRNA expression levels of 6 osteoblast-related genes on the surface of Si_3N_4–G are higher than those on the surface of Si_3N_4 at each time point.

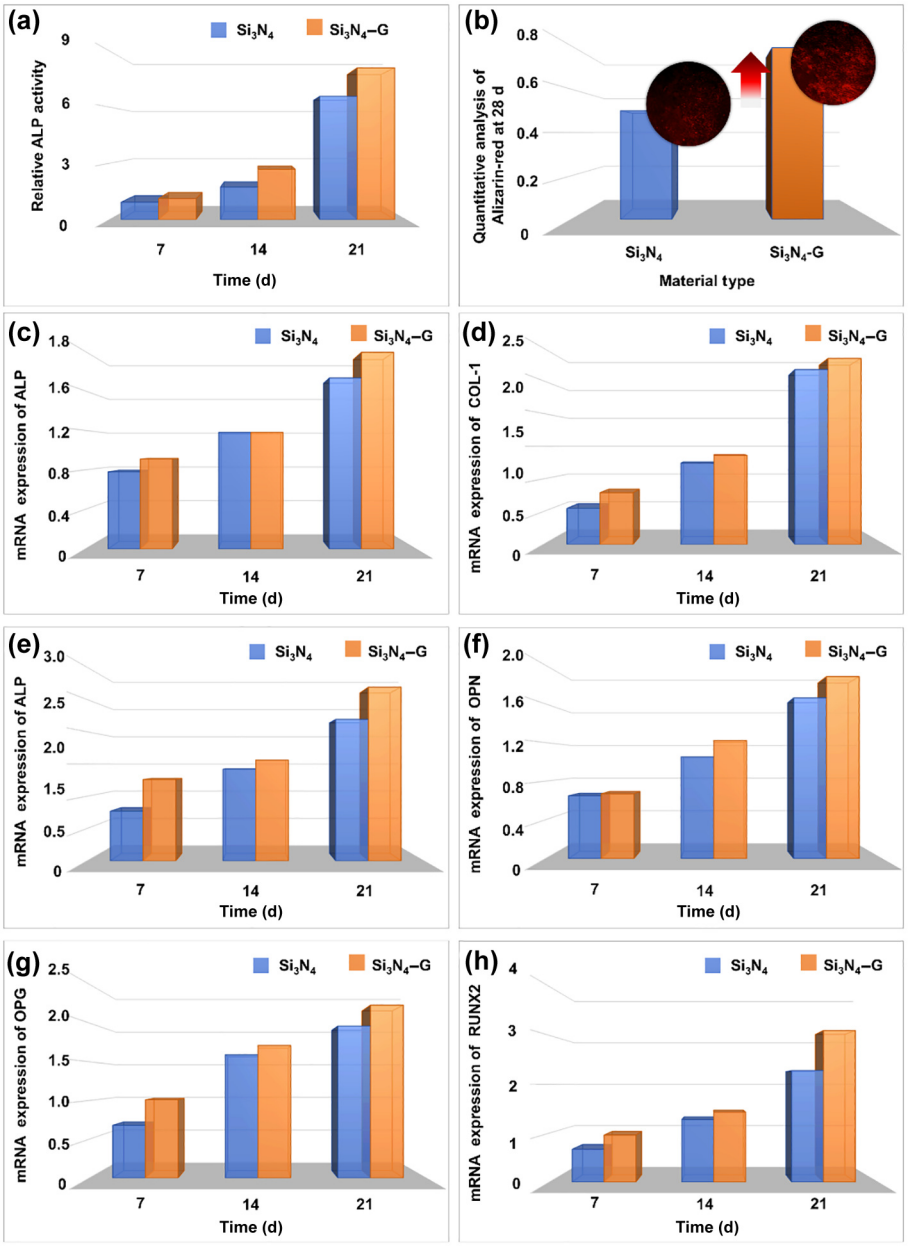

Fig. 10 Osteoinductive differentiation of MC3T3-E1 cells grown on Si_3N_4 and Si_3N_4–G: (a) ALP cell staining assays; (b) quantitative analysis of Alizarin red and stained images of mineralized cell nodules; (c–h) relative mRNA expression of 6 osteogenesis-related genes.

In summary, the approach taken in this study served to enhance the mechanical and biological performance of Si_3N_4, offering new insights into the application of ceramic composites in bone tissue engineering.

Acknowledgements

This work is supported by the National Natural Science Foundation of China (No. 52172133) and the Heilongjiang Touyan Team (No. HITTY-20190034).

Declaration of competing interest

The authors have no competing interests to declare that are relevant to the content of this article.

References

[1] Pezzotti G, Marin E, Adachi T, *et al.* Bioactive silicon nitride: A new therapeutic material for osteoarthropathy. *Sci Rep* 2017, **7**: 44848.

[2] Wang ZY, Li L, Deng B, *et al.* Research progress of silicon nitride-based human implanted materials. *Adv Ceram* 2019, **40**: 135–149. (in Chinese).

[3] Pezzotti G. Silicon nitride: A bioceramic with a gift. *ACS Appl Mater Inter* 2019, **11**: 26619–26636.

[4] Pezzotti G, Bock RM, McEntire BJ, *et al. In vitro* antibacterial activity of oxide and non-oxide bioceramics for arthroplastic devices: I. *In situ* time-lapse Raman spectroscopy. *Analyst* 2018, **143**: 3708–3721.

[5] Li JS, Yu QP, Li D, *et al.* Formation of hierarchical Si_3N_4 foams by protein-based gelcasting and chemical vapor infiltration. *J Adv Ceram* 2021, **10**: 187–193.

[6] Xu SS, Zhou XN, Zhi Q, *et al.* Anisotropic, biomorphic cellular Si_3N_4 ceramics with directional well-aligned nanowhisker arrays based on wood-mimetic architectures. *J Adv Ceram* 2022, **11**: 656–664.

[7] Krstic Z, Krstic VD. Silicon nitride: The engineering material of the future. *J Mater Sci* 2012, **47**: 535–552.

[8] Sun Y, Meng QC, Jia DC, *et al.* Effect of hexagonal BN on the microstructure and mechanical properties of Si_3N_4 ceramics. *J Mater Process Tech* 2007, **182**: 134–138.

[9] Li YF, Liu P, Wang XD, *et al.* Interface structure and formation mechanism of BN/intergranular amorphous phase in pressureless sintered Si_3N_4/BN composites. *Scripta Mater* 2010, **63**: 185–188.
[10] Hu HL, Yao DX, Xia YF, *et al.* Fabrication and mechanical properties of SiC reinforced reaction-bonded silicon nitride based ceramics. *Ceram Int* 2014, **40**: 4739–4743.
[11] Zheng DH, Li XQ, Tang Y, *et al.* WC–Si_3N_4 composites prepared by two-step spark plasma sintering. *Int J Refract Met H* 2015, **50**: 133–139.
[12] Cho J, Boccaccini AR, Shaffer MSP. Ceramic matrix composites containing carbon nanotubes. *J Mater Sci* 2009, **44**: 1934–1951.
[13] Wolfrum AK, Quitzke C, Matthey B, *et al.* Wear behavior of diamond–silicon nitride composites sintered with FAST/SPS. *Wear* 2018, **396**: 172–181.
[14] Moya JS, Lopez-Esteban S, Pecharromán C. The challenge of ceramic /metal microcomposites and nanocomposites. *Prog Mater Sci* 2007, **52**: 1017–1090.
[15] Wu J, Liu YJ, Zhang H, *et al.* Silicon nitride as a potential candidate for dental implants: Osteogenic activities and antibacterial properties. *J Mater Res* 2021, **36**: 1866–1882.
[16] Gorth DJ, Puckett S, Ercan B, *et al.* Decreased bacteria activity on Si_3N_4 surfaces compared with PEEK or titanium. *Int J Nanomed* 2012, **7**: 4829–4840.
[17] Bock RM, Jones EN, Ray DA, *et al.* Bacteriostatic behavior of surface modulated silicon nitride in comparison to polyetheretherketone and titanium. *J Biomed Mater Res A* 2017, **105**: 1521–1534.
[18] Ishikawa M, de Mesy Bentley KL, McEntire BJ, *et al.* Surface topography of silicon nitride affects antimicrobial and osseointegrative properties of tibial implants in a murine model. *J Biomed Mater Res A* 2017, **105**: 3413–3421.
[19] Pezzotti G, Bock RM, McEntire BJ, *et al.* Silicon nitride bioceramics induce chemically driven lysis in porphyromonas gingivalis. *Langmuir* 2016, **32**: 3024–3035.
[20] Bozkurt D, Akarsu MK, Akin I, *et al.* Phase analysis, mechanical properties and *in vitro* bioactivity of graphene nanoplatelet-reinforced silicon nitride-calcium phosphate composites. *J Asian Ceram Soc* 2021, **9**: 471–486.
[21] Liu ZY, Fu S, Liu XM, *et al.* Small size, big impact: Recent progress in bottom-up synthesized nanographenes for optoelectronic and energy applications. *Adv Sci* 2022, **9**: 2106055.
[22] Dreyer DR, Park S, Bielawski CW, *et al.* The chemistry of graphene oxide. *Chem Soc Rev* 2010, **39**: 228–240.
[23] Szabó T, Berkesi O, Forgó P, *et al.* Evolution of surface functional groups in a series of progressively oxidized graphite oxides. *Chem Mater* 2006, **18**: 2740–2749.
[24] Gao W, Alemany LB, Ci LJ, *et al.* New insights into the structure and reduction of graphite oxide. *Nat Chem* 2009, **1**: 403–408.
[25] Zhang YP, Li DL, Tan XJ, *et al.* High quality graphene sheets from graphene oxide by hot-pressing. *Carbon* 2013, **54**: 143–148.
[26] Pham VTH, Truong VK, Quinn MDJ, *et al.* Graphene induces formation of pores that kill spherical and rod-shaped bacteria. *ACS Nano* 2015, **9**: 8458–8467.
[27] Mohammed H, Kumar A, Bekyarova E, *et al.* Antimicrobial mechanisms and effectiveness of graphene and graphene-functionalized biomaterials. A scope review. *Front Bioeng Biotechnol* 2020, **8**: 465.
[28] Luong-Van EK, Madanagopal TT, Rosa V. Mechanisms of graphene influence on cell differentiation. *Mater Today Chem* 2020, **16**: 100250.
[29] Akhavan O, Ghaderi E, Esfandiar A. Wrapping bacteria by graphene nanosheets for isolation from environment, reactivation by sonication, and inactivation by near-infrared irradiation. *J Phys Chem B* 2011, **115**: 6279–6288.
[30] Pandit S, Cao ZJ, Mokkapati VRSS, *et al.* Vertically aligned graphene coating is bactericidal and prevents the formation of bacterial biofilms. *Adv Mater Interfaces* 2018, **5**: 1701331.
[31] Gurunathan S, Han JW, Dayem AA, *et al.* Oxidative stress-mediated antibacterial activity of graphene oxide and reduced graphene oxide in *Pseudomonas aeruginosa*. *Int J Nanomed* 2012, **7**: 5901–5914.
[32] West JD, Marnett LJ. Endogenous reactive intermediates as modulators of cell signaling and cell death. *Chem Res Toxicol* 2006, **19**: 173–194.
[33] Lee WC, Lim CH, Shi H, *et al.* Origin of enhanced stem cell growth and differentiation on graphene and graphene oxide. *ACS Nano* 2011, **5**: 7334–7341.
[34] Daneshmandi L, Barajaa M, Tahmasbi Rad A, *et al.* Graphene-based biomaterials for bone regenerative engineering: A comprehensive review of the field and considerations regarding biocompatibility and biodegradation. *Adv Healthc Mater* 2021, **10**: e2001414.